




Reconnection Front Associated with Asymmetric Magnetic Reconnection: Particle-in-cell Simulations

Liangjin Song^{1,2} , Meng Zhou^{1,2,4}, Yongyuan Yi^{1,2}, Xiaohua Deng², and Zhihong Zhong^{2,3}

¹ Department of Physics, School of Science, Nanchang University, Nanchang 330031, People's Republic of China; monmomentum82@gmail.com

² Institute of Space Science and Technology, Nanchang University, Nanchang 330031, People's Republic of China

³ School of Resources Environmental and Chemical Engineering, Nanchang University, Nanchang 330031, People's Republic of China

Received 2019 May 11; revised 2019 July 25; accepted 2019 July 26; published 2019 August 12

Abstract

Reconnection front (RF) has frequently been observed in the magnetotail and is well known as the dipolarization front in the near-Earth tail. Whether the RF exists in reconnection with distinct plasma/field properties across the reconnecting current sheet (i.e., asymmetric reconnection) is unknown yet. In this Letter, we use 2.5D particle-in-cell simulations to investigate the properties of RF in asymmetric reconnection and compare to RFs in symmetric reconnection. We find that RF is a robust structure in asymmetric reconnection. Its moving speed and thickness are smaller than those in symmetric reconnection. Its properties, such as the current density, electromagnetic field structure, are examined. Some features of RF in asymmetric reconnection are drastically different than those in symmetric reconnection. These results are of great help for studying RF in plasma environments with asymmetric reconnection, such as Earth's magnetopause.

Unified Astronomy Thesaurus concepts: [Solar magnetic reconnection \(1504\)](#); [Astronomical simulations \(1857\)](#); [Planetary boundary layers \(1245\)](#)

1. Introduction

Magnetic reconnection refers to the process of spontaneous or forced disconnection and reconnection of magnetic field lines in a magnetized plasma with finite conductivity, accompanied by an explosive release of magnetic energy, causing acceleration and heating of plasma. It is widely found in nature and laboratory plasmas, such as the solar corona (Priest 2000), Earth's magnetosphere (Paschmann et al. 1979; Deng & Matsumoto 2001; Vaivads et al. 2004), tokamak, etc. (Ono et al. 2012).

Reconnection produces magnetic structures that propagate outward from the reconnection site and stir the ambient plasma. Reconnection front (RF) is the leading boundary of the reconnection outflow. It is characterized by the enhancement of the reconnected magnetic field component. In the magnetotail, RF is also known as the dipolarization front, which is the leading boundary of dipolarizing flux bundles and embedded in fast flows generated by magnetotail reconnection (e.g., Nakamura et al. 2002; Runov et al. 2009; Zhou et al. 2009, 2011; Liu et al. 2013). Sitnov et al. (2009) suggested that RF is an intrinsic product of transient reconnection. It can be formed by the interaction between reconnection outflow and ambient plasma (Fu et al. 2011, 2013; Vapirev et al. 2013). An alternative formation mechanism is that RFs result from the erosion of earthward moving flux ropes by reconnection with the geomagnetic field (Man et al. 2018). RF is a boundary layer separating the intruding hot tenuous plasma and the ambient cold dense plasma (Runov et al. 2011). It is also a current sheet with thickness on the order of the ion inertial length or Larmor radius. Hall electric field normal to the front surface is formed in such a thin current sheet (Zhou et al. 2009; Fu et al. 2012). Recent magnetospheric multiscale (MMS) observations show that RF consisted of electron-scale substructures (Liu et al. 2018; Zhou et al. 2019).

It has been suggested that RFs are crucial in the energy budget of magnetotail. A significant amount of magnetic energy was

transferred to the plasmas ($\mathbf{J} \cdot \mathbf{E} > 0$) at the RFs (Huang et al. 2012, 2015a; Angelopoulos et al. 2013). Ions are reflected at RFs and accelerated by the motional electric field (Zhou et al. 2010; Drake et al. 2014). RFs are also associated with energetic electrons (Zhou et al. 2009; Deng et al. 2010; Fu et al. 2011). It is suggested that the main acceleration mechanism for electrons is the adiabatic betatron and Fermi acceleration (Fu et al. 2011; Birm et al. 2013). However, plasma waves, such as lower hybrid drift waves, whistler waves, and magnetosonic waves, may contribute to the nonadiabatic acceleration of electrons at RFs (Zhou et al. 2009, 2014b; Deng et al. 2010; Khotyaintsev et al. 2011; Huang et al. 2012; Hwang et al. 2014; Divin et al. 2015; Li et al. 2015).

RFs have frequently been observed throughout the near-Earth magnetotail, where reconnection generally occurs in the neutral sheet with symmetric inflow boundaries. However, reconnection usually occurs in an asymmetric current sheet in nature, such as in Earth's magnetopause (e.g., Burch et al. 2016; Zhou et al. 2016). Important questions related to the RF and asymmetric reconnection are: Are there RFs in asymmetric reconnection? If there are, then what are the properties of these RFs? In this Letter, we address these open questions by 2.5D particle-in-cell (PIC) simulations.

2. Simulation Model

A 2.5D electromagnetic PIC simulation code is used for this study (Zhou et al. 2012a, 2012b, 2014a; Huang et al. 2015b). Our code employs mostly the same method as previous explicit PIC codes. For instance, the electromagnetic fields are defined on the Yee lattice (Yee 1966). We solve the relativistic Lorentz equation to update particles' speed with the Buneman-Boris method (Birdsall & Langdon 1985). The continuity equation is solved to keep Poisson's equation satisfied to near machine precision (Villasenor & Buneman 1992).

We have performed a simulation with asymmetric inflow boundaries. Two Harris current sheets initialize the magnetic

⁴ Corresponding author.

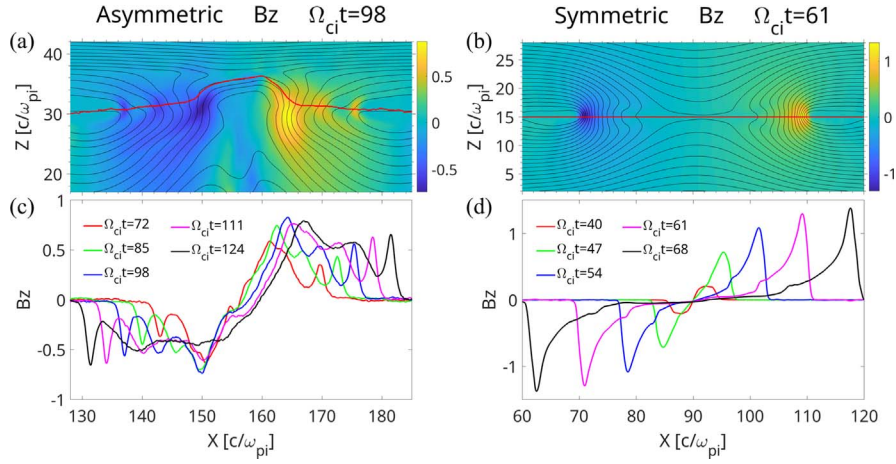


Figure 1. Left column shows the results from the asymmetric reconnection, while the right column shows the results from the symmetric reconnection. Color codings in panels (a) and (b) represent B_z , and the superposed black contours are magnetic field lines. The red curves denote the $B_x = 0$ surface. Panels (c) and (d) show the profiles of B_z along x across the center of the RF at five different instants. The curves in panel (c) are taken at $z = 30.10, 30.01, 30.80, 29.93, 29.66d_i$, respectively, due to the weak vertical motion of the $B_x = 0$ surface in the Z direction, while all the curves in panel (d) are along $z = 15d_i$.

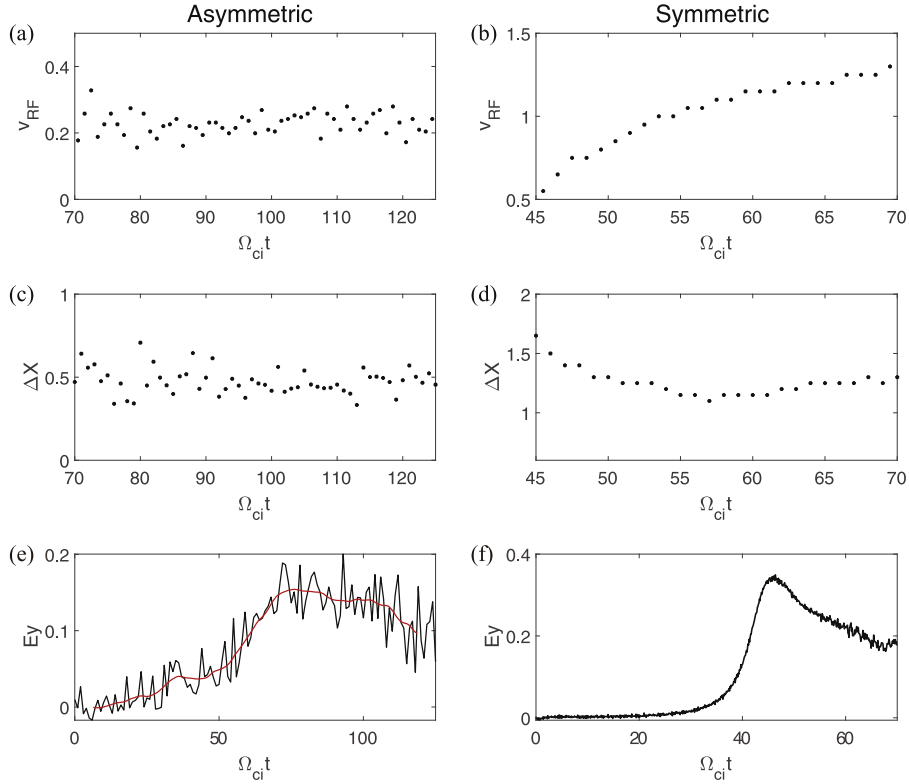


Figure 2. RF’s velocity (panels (a) and (b)), the thickness (panels (c) and (d)), and the reconnection rate (panels (e) and (f)) as a function of time. The left (right) column shows the results from the asymmetric (symmetric) reconnection.

field, plasma density, and temperature (e.g., Malakit et al. 2010). The ratio of the number density across the current sheet is $n_1/n_2 = 7$, the ratio of temperature is $T_2/T_1 = 6$, and the ratio of magnetic field strength is $B_2/B_1 = 1.5$, where “1” represents the side with cold dense plasma and weaker magnetic field (resembling the magnetosheath), while “2” represents the side with hot tenuous plasma and stronger magnetic field (resembling the magnetosphere). The mass ratio is $m_i/m_e = 100$, and the initial temperature ratio is $T_i/T_e = 2$. The number of grids is 4800×2400 , and 150 particles per grid are used. Periodic boundary conditions are used in both directions. In addition,

we performed a simulation of symmetric reconnection as a comparison. The number of grids and particles per grid are the same as those of asymmetric reconnection. We set the initial guide field as zero in both cases.

All physical quantities are normalized as follows. The magnetic field is normalized to the asymptotic magnetic field B_0 ($B_0 = B_1$ in the asymmetric case). The time is normalized by the ion gyroperiod Ω_{ci}^{-1} based on B_0 . The plasma density is normalized to n_1 (asymmetric case) or n_0 (symmetric case). The length is normalized by the ion inertial length d_i based on n_1 (asymmetric case) or n_0 (symmetric case). In the asymmetric

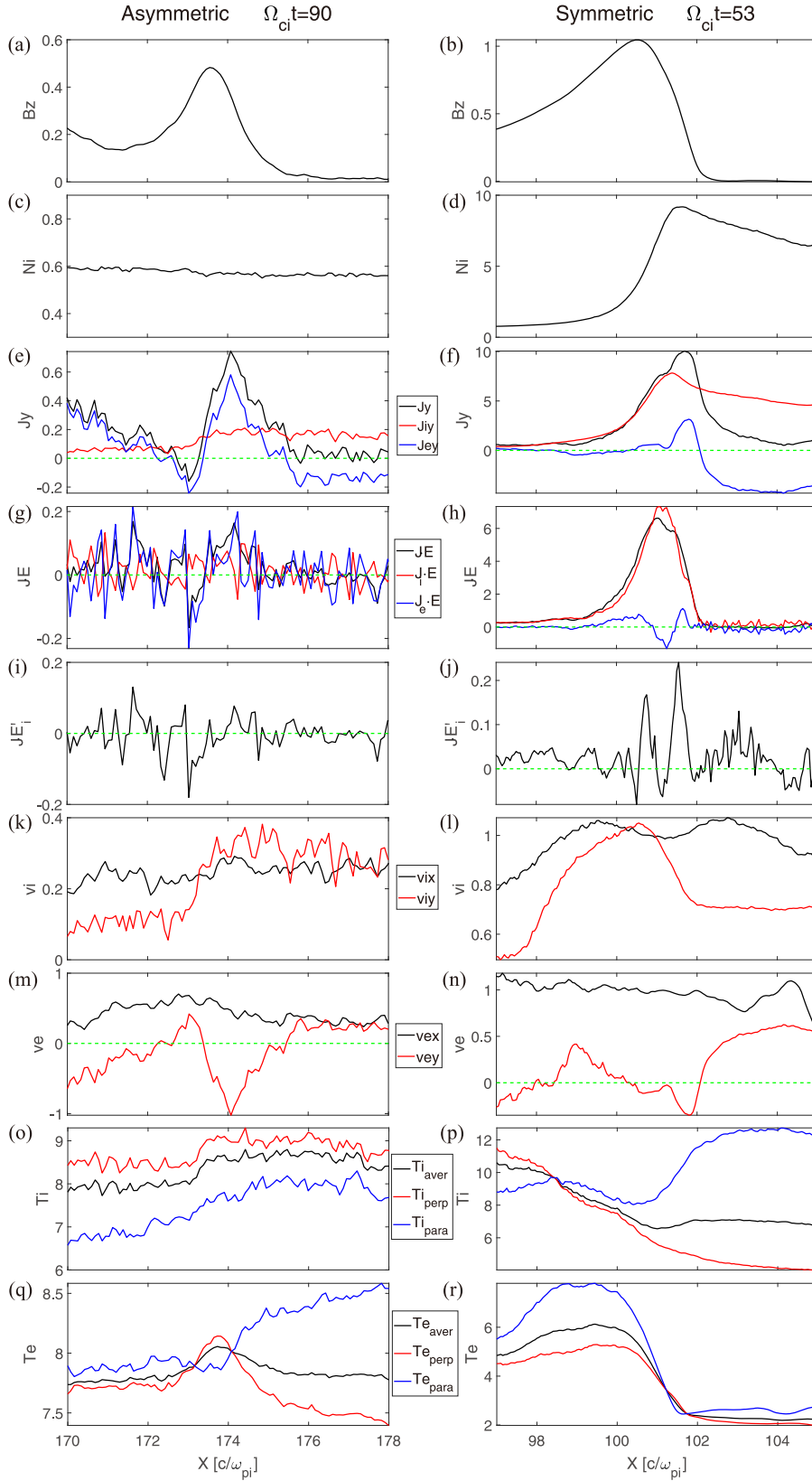


Figure 3. Electromagnetic and plasma properties across the RFs along the X direction. Left column shows the results from the asymmetric reconnection at time $t = 90\Omega_{ci}^{-1}$, while the right column is for the symmetric reconnection at $t = 53\Omega_{ci}^{-1}$. From the top to the bottom are ((a)–(b)) magnetic field B_z ; ((c)–(d)) plasma density N_i ; ((e)–(f)) current density J_y (black), J_{iy} (red), and J_{ey} (blue); ((g)–(h)) energy conversion $\mathbf{J} \cdot \mathbf{E}$ (black), $\mathbf{J}_i \cdot \mathbf{E}$ (red), and $\mathbf{J}_e \cdot \mathbf{E}$ (blue); ((i)–(j)) energy dissipation $\mathbf{J} \cdot \mathbf{E}_i'$; ((k)–(l)) ion bulk velocity v_{ix} and v_{iy} ; ((m)–(n)) electron bulk velocity v_{ex} and v_{ey} ; ((o)–(p)) ion temperatures; and ((q)–(r)) electron temperatures. The average ion temperature $T_{i,aver}$ is equal to $(T_{i,para} + 2T_{i,perp})/3$, and the average electron temperature $T_{e,aver}$ is equal to $(T_{e,para} + 2T_{e,perp})/3$.

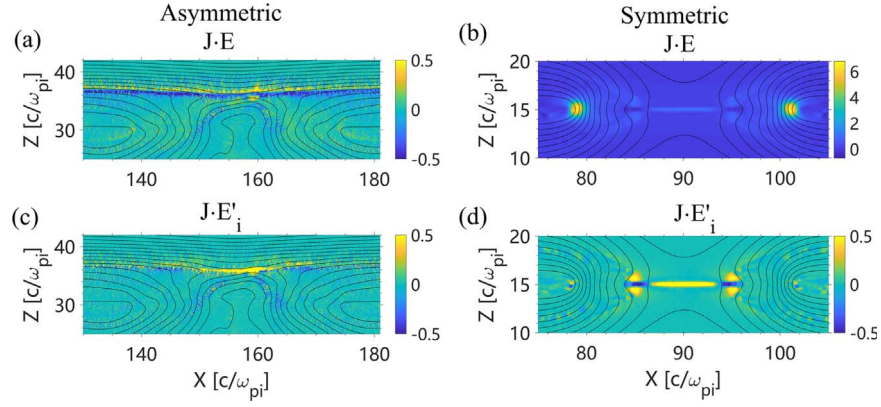


Figure 4. $\mathbf{J} \cdot \mathbf{E}$ (panels (a) and (b)) and $\mathbf{J} \cdot \mathbf{E}'_i$ (panels (c) and (d)). Left column shows the results from the asymmetric reconnection at time $t = 90\Omega_{ci}^{-1}$, while the right column is for the symmetric reconnection at $t = 53\Omega_{ci}^{-1}$.

simulation, $d_i = 23$ is the asymptotic ion inertial length on the high-density side. In the symmetric simulation, $d_i = 40$ is the ion inertial length in the central current sheet. Accordingly, the simulation domain is $208.7d_i \times 104.3d_i$ for the asymmetric cases and $120d_i \times 60d_i$ for the symmetric case. The velocity is normalized to the Alfvén speed v_A on the high-density side (asymmetric case) or based on B_0 and n_0 (symmetric case). The current density is normalized to qn_1v_A (asymmetric case) or qn_0v_A (symmetric case). The electric field is normalized by B_1v_A (asymmetric case) or B_0v_A (symmetric case). The temperature is normalized to the initial electron temperature T_1 on the high-density side (for the symmetric case the initial temperature is uniform).

3. On the RF in Asymmetric Reconnection

First, we check whether RFs exist in asymmetric reconnection or not. Figures 1(a) and (b) display the magnetic field B_z at $t = 98\Omega_{ci}^{-1}$ from the asymmetric reconnection and $t = 61\Omega_{ci}^{-1}$ from the symmetric reconnection, respectively. The red curves in these two panels mark the location of $B_x = 0$. It is noticeable that $B_x = 0$ in the asymmetric case is a curve rather than a straight line in the symmetric case. Figure 1(b) shows a positive (negative) B_z enhancement on the $+X$ ($-X$) side of the X line. The two $|B_z|$ enhancements propagate away from the X line as time progresses, which is clearly demonstrated in Figure 1(d). This is the RF as reported in previous PIC simulations (Sitnov et al. 2009; Wu & Shay 2012).

According to previous simulations and magnetotail observations, RF is a coherent structure characterized by B_z enhancement. It is created at the X line and propagates outward, existing for a long period (e.g., Runov et al. 2009). Figure 1(a) shows a few $|B_z|$ enhancements on each side of the X line in the asymmetric case. We see that the B_z enhancements are initiated near the X line, then propagate away from the X line and grow in magnitude (Figure 1(c)). This is consistent with our definition of RF. Hence, we conclude that RFs are also coherent structures produced by asymmetric reconnection. The peak value of B_z at the RF in the symmetric case is about twice of that in the asymmetric case. Note that there is a pair of structures with large-amplitude B_z near the X line in the asymmetric case, but they barely propagate.

Figure 2 shows the velocity and thickness of the RF on the $+X$ side of the X line and the reconnection rate as a function of time for the asymmetric (left) and symmetric case (right). The

RF's thickness and velocity are shown for the time interval when it is visible in the simulation. In the asymmetric case, the propagating speed (Figure 2(a)) of the RF is stable, around $0.2v_A$. While in the symmetric case, the velocity (Figure 2(b)) of the RF gradually increases from $0.5v_A$ and tends to be stabilized around $1.2v_A$. The speed of RF in the asymmetric reconnection is only a fraction of that in the symmetric reconnection. The thicknesses of the RFs in both the asymmetric (Figure 2(c)) and symmetric (Figure 2(d)) cases are relatively stable, around $0.5d_i$ and $1.3d_i$, respectively. Here the RF's thickness is determined as the distance between the position of B_z maximum and the position where the value of B_z is equal to $1/e$ of the $B_{z,\max}$.

Figures 2(e) and (f) display the electric field E_y at the X line, which represents the reconnection rate. The red curve in Figure 2(e) is the smoothed E_y . The reconnection rates are fast in both cases, with the rate is higher in the symmetric case than in the asymmetric case. The rapid increase of reconnection rate in the symmetric reconnection starts approximately at $t = 35\Omega_{ci}^{-1}$. It reaches peak at around $t = 42\Omega_{ci}^{-1}$. The RF begins to propagate away from the X line at about $t = 45\Omega_{ci}^{-1}$. During the outward propagation of RF, the reconnection rate gradually decreases. After $t = 70\Omega_{ci}^{-1}$, the reconnection starts to be affected by the periodic boundary condition because the two reconnection outflows encounter with each other. In the asymmetric reconnection, the onset of the fast reconnection occurs at approximately $t = 30\Omega_{ci}^{-1}$. At about $t = 45\Omega_{ci}^{-1}$, the RF begins to propagate outward, and the reconnection rate begins to increase gradually. At $t = 70\Omega_{ci}^{-1}$, a new structure with B_z enhancement is created behind the RF and propagates outward. Then the reconnection rate slowly falls and the RF's speed reaches stable.

In the following we compare the properties of the RF between the symmetric and asymmetric cases. Figure 3 shows the magnetic field, electric current density, and plasma properties across the RF for both the asymmetric (left column) and symmetric (right column) cases. The RF is at $X \approx 174d_i$ in the asymmetric reconnection (Figure 3(a)), while it is at $X \approx 101d_i$ (Figure 3(b)) in the symmetric case. Both RFs are embedded within fast flows. The ion flows are not only in the X direction, but have a large component in the Y direction. The electron bulk velocities in the X direction are similar to the ion bulk velocities. However, v_{ey} is obviously different to v_{iy} in both cases. The plasma density changes little across the RF in the asymmetric reconnection (Figure 3(c)). However, in the

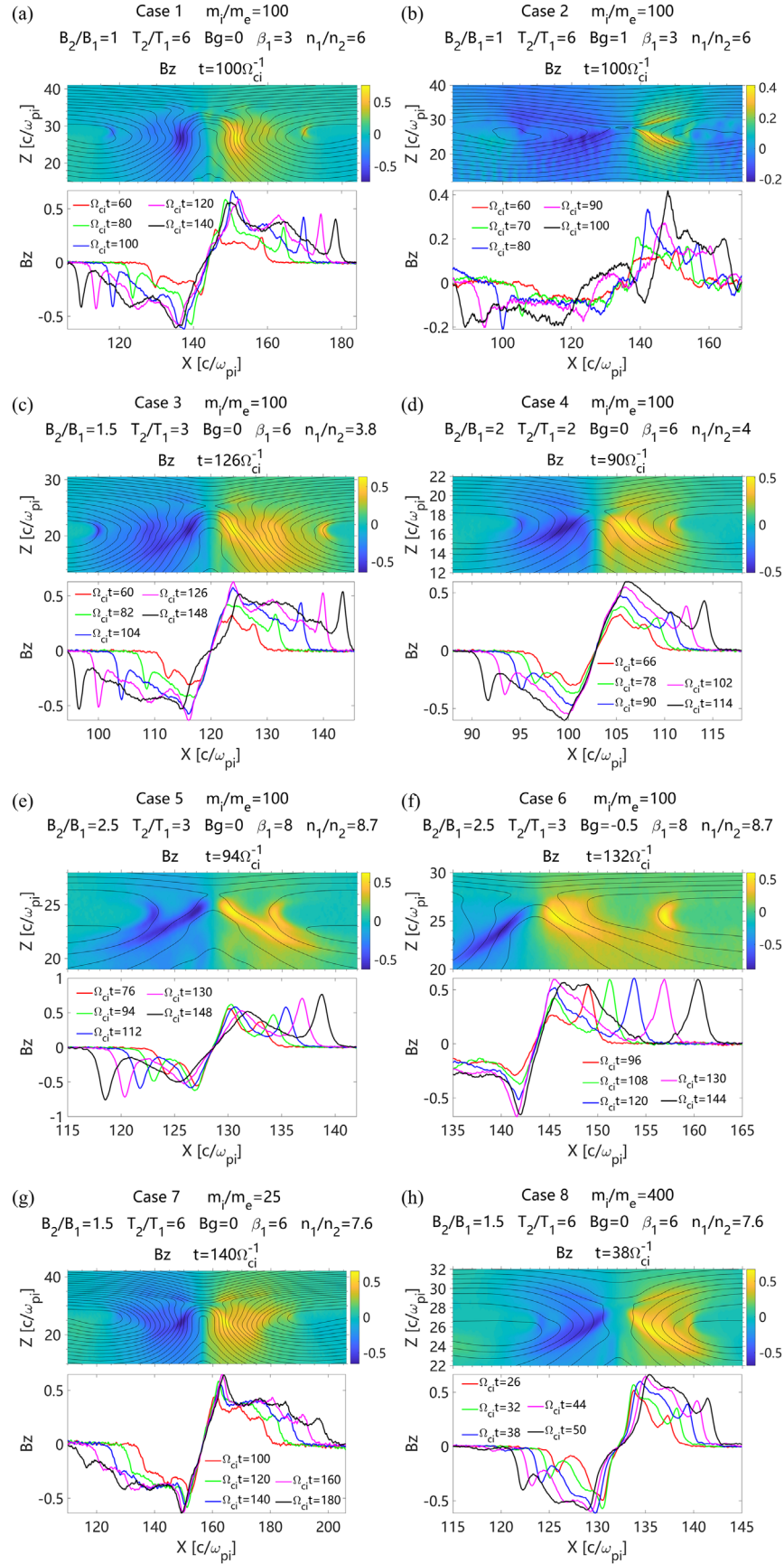


Figure 5. Simulation results from the additional eight runs with different initial conditions. Each panel consists of two plots. The upper plot shows the magnetic field B_z in the X - Z plane at the time when the RFs are fully developed in the simulation. The lower plot shows the profiles of B_z in the X direction across the center of the RF at five different instants.

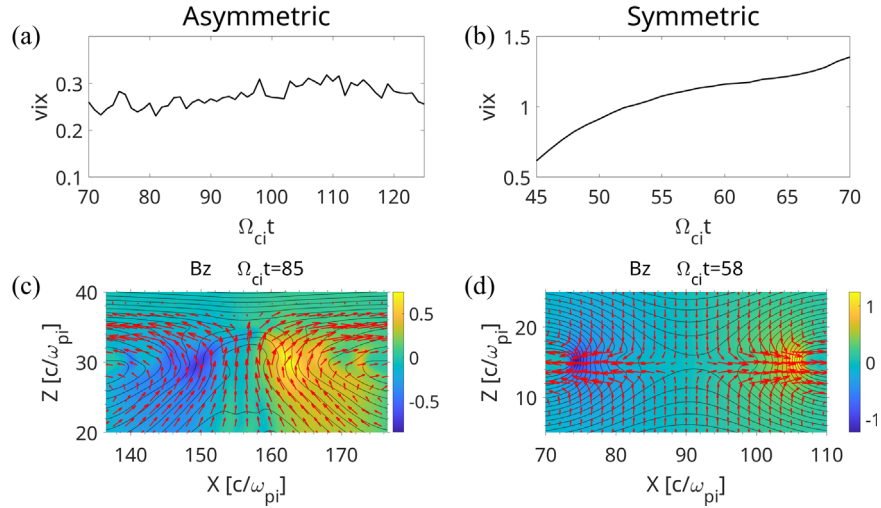


Figure 6. Panels (a) and (b) display the time variation of v_{ix} at the RF. Panels (c) and (d) display the magnetic field B_z (color codings) in the X - Z plane. The superposed black curves denote the magnetic field lines, and the red arrows denote the ion flow vectors, the length of which is proportional to the flow speed. The left (right) column shows the results from the asymmetric (symmetric) reconnection.

symmetric reconnection, the plasma density gradually increases toward the RF and drops sharply behind the front, which forms a strong density gradient at the front. The peaks of magnetic field B_z and plasma density N_i do not coincide with each other in the symmetric case. These features are consistent with the observations of RFs in magnetotail (Ohtani et al. 2004; Runov et al. 2009).

We see that J_y increases at the RFs in both the asymmetric (Figure 3(e)) and symmetric reconnection (Figure 3(f)). In the asymmetric reconnection, the current J_y is mainly carried by electrons as $|v_{ey}|$ is much greater than $|v_{iy}|$. This is in contrast with the symmetric case, in which the current J_y is mainly carried by ions as $|v_{iy}|$ is larger than $|v_{ey}|$. Figures 3(g) and (h) show the magnetic energy conversion rate $\mathbf{J} \cdot \mathbf{E}$ associated with the RFs. In the symmetric reconnection, magnetic energy mainly goes to ions as $\mathbf{J}_i \cdot \mathbf{E} \gg \mathbf{J}_e \cdot \mathbf{E}$. This is consistent with recent Cluster spacecraft observations in the magnetotail (Khotyaintsev et al. 2017). In contrast, $\mathbf{J}_i \cdot \mathbf{E} \approx \mathbf{J}_e \cdot \mathbf{E}$ at the RF in the asymmetric case and the total energy conversion $\mathbf{J} \cdot \mathbf{E}$ is much smaller than that in the symmetric reconnection. Moreover, $\mathbf{J} \cdot \mathbf{E}$ does not show a clear peak at the RF. Figures 3(i) and (j) show $\mathbf{J} \cdot \mathbf{E}'_i$, where $\mathbf{E}'_i = \mathbf{E} + \mathbf{v}_i \times \mathbf{B}$. It represents the energy conversion in the ion frame and has widely been used to quantify the magnetic energy dissipation in collisionless plasmas (e.g., Zenitani et al. 2011). Because of the quasi-neutrality ($n_e \approx n_i$), $\mathbf{J} \cdot \mathbf{E}'_e \approx \mathbf{J} \cdot \mathbf{E}'_i$, here we show $\mathbf{J} \cdot \mathbf{E}'_i$ only. Although $\mathbf{J} \cdot \mathbf{E}'_i$ exhibits two peaks at the RF in the symmetric case, its magnitude is much smaller than $\mathbf{J} \cdot \mathbf{E}$ at the RF. $\mathbf{J} \cdot \mathbf{E}'_i$ at RF in the asymmetric case is comparable to the background value. Figure 4 displays the 2D spatial distribution of $\mathbf{J} \cdot \mathbf{E}$ (Figures 4(a) and (b)) and $\mathbf{J} \cdot \mathbf{E}'_i$ (Figures 4(c) and (d)) for both the asymmetric (left column) and symmetric (right column) cases. We see that the energy conversion $\mathbf{J} \cdot \mathbf{E}$ and dissipation $\mathbf{J} \cdot \mathbf{E}'_i$ at the RF in the asymmetric case is insignificant compared to the background noise level. Energy conversion and dissipation in asymmetric reconnection mainly occur at the low-density separatrix region. This is drastically distinct from $\mathbf{J} \cdot \mathbf{E}$ and $\mathbf{J} \cdot \mathbf{E}'_i$ in symmetric reconnection, where positive $\mathbf{J} \cdot \mathbf{E}$ predominantly locates

around the RF and positive $\mathbf{J} \cdot \mathbf{E}'_i$ mainly locates near the X line.

The average ion temperature decreases behind the RF in the asymmetric case (Figure 3(o)). While in the symmetric reconnection, it decreases slightly at the RF and gradually increases behind the RF. The average electron temperature enhances locally (Figure 3(q)) in the asymmetric reconnection, while it increases substantially behind the RF in the symmetric reconnection. In the asymmetric reconnection, the ion temperature is always anisotropic with $T_{i\text{perp}} > T_{i\text{para}}$ (Figure 3(o)), while the electrons have a local anisotropy with $T_{e\text{perp}} > T_{e\text{para}}$ at the RF and exhibit $T_{e\text{para}} > T_{e\text{perp}}$ surrounding the RF (Figure 3(q)). The electron temperature anisotropy in the symmetric reconnection (Figure 3(r)) is similar to that in the asymmetric reconnection, while the ion temperature shows $T_{i\text{para}} > T_{i\text{perp}}$ preceding the RF in the symmetric reconnection (Figure 3(p)), which is opposite to that in the asymmetric case.

4. Robustness

To determine whether RF is a robust structure in asymmetric reconnection, we have performed eight additional simulations with different initial conditions by varying the initial ratios of the magnetic field, plasma density, and temperature on the two sides of the current sheet, the mass ratios, and the guide field strengths. Figure 5 displays the magnetic field B_z for all eight cases. The ratio of magnetic field varies from 1 to 2.5. We have imposed initial guide field in cases 2 and 6. The mass ratio of case 7 and case 8 are 25 and 400, respectively, while the mass ratios for the other cases are 100. The detailed parameters of these cases are listed in each panel in Figure 5.

Similar to the RF shown in Section 3, all these cases reproduce structures with evident B_z enhancement that propagate outward. Therefore, we believe that RF is a robust structure in asymmetric reconnection. The magnetic field profiles of these RFs are different, which may be caused by the different initial asymmetry settings. It is notable that reconnections in case 2 and case 6 have asymmetric open angles in the outflow direction, which is caused by the advection of the X line as a result of diamagnetic drift due to the guide field (Swisdak et al. 2003). The RF is also

asymmetric in the outflow direction in case 6, namely, it appears only on the right-hand side of the X line. However, RFs exist on both sides of the X line in case 2, which also has an initial guide field. The influence of guide field on the RFs in asymmetric reconnection needs further investigating. Our preliminary results suggest that the existence of RF in asymmetric reconnection does not depend on the mass ratio. However, mass ratio may determine the evolution and amplitude of RF since the growth rate of tearing instability, which is likely the driven mode of RF, depends on the mass ratio (e.g., Daughton 1999).

5. Discussion and Conclusion

In this Letter, we study the RF in asymmetric reconnection by performing a series of 2.5D PIC simulations. We show that RFs exist in asymmetric magnetic reconnection. They are located around the neutral surface in the outflow region. Some features of the RF in asymmetric reconnection are drastically different from those of the RF in symmetric reconnection. In particular, the velocity and thickness of the RF are smaller in asymmetric reconnection than in symmetric reconnection. RF is a current layer in asymmetric reconnection since the current density J_y reaches peak at the RF and is mainly carried by electrons, whereas J_y at the RF in symmetric reconnection is mainly carried by ions. The energy conversion $\mathbf{J} \cdot \mathbf{E}$ and dissipation $\mathbf{J} \cdot \mathbf{E}'_i$ at the RF in asymmetric reconnection are negligible because their values are insignificant compared to the background noise, while those in symmetric reconnection are significant. The energy conversion $\mathbf{J} \cdot \mathbf{E}$ is primarily attributed to $\mathbf{J}_i \cdot \mathbf{E}$ in symmetric reconnection. RF in asymmetric reconnection is not a boundary layer as it is in symmetric reconnection because the plasma density and temperature do not change significantly across the RF.

Figure 6 shows the ion speed at the RF and the ion flow vectors in the X - Z plane. The X point and the stagnation point are separated along the Z direction in asymmetric reconnection (Cassak & Shay 2007). The ion outflow speed is the largest around the magnetic separatrix on the low-density side, where the magnetic field is mainly parallel to the ion flow. For both cases, the ion flow is primarily perpendicular to the magnetic field at the RFs, which is in the center of the outflow region (Figure 6(d)).

The propagation speed of the RF is close to v_{ix} at the RF in both cases (Figures 2 and 6). Near the X line in the asymmetric reconnection, ions almost move in the Z direction (Figure 6(c)). The flux pileup region near the X line, which is manifested as the nearly standing B_z enhancement, slowly expands as the evolution of reconnection because of the magnetic tension and pressure. When the region expands to the position where v_{ix} dominates over v_{iz} , a structure with B_z enhancement, whose moving speed is approximately equal to that of the ion outflow, propagates outward from the X line. This process repeatedly occurs as reconnection is going on, which leads to new B_z humps behind the RF (shown in Figure 1(c)).

This study can serve as a guidance for detecting RF in asymmetric reconnection, such as that which occurs in Earth's magnetopause, where MMS, Cluster, THEMIS, and Double star missions have already accumulated large amounts of data. The RFs in our simulations are confined in the outflow region, closer to the side with weaker magnetic field or denser plasmas. Moreover, we see that the RF has limited size around the red

curve in Figure 1(a); hence, satellites should be close to the magnetopause current sheet in order to observe the RF.

Finally, we should note that there are some limitations when applying our results to Earth's magnetopause. Some features of the real magnetopause are missing in our simulations. (i) Magnetopause is a curved surface rather than a plane as assumed in our simulation. Accordingly, the initial magnetic field lines are curved instead of straight lines. (ii) It is known that solar wind compresses the magnetopause and imposes a driven electric field, which is missing here, at the magnetosheath boundary. (iii) We did not include shear flows in our simulation. In short, the realistic magnetopause reconnection is much more complicated than we simulated here. We plan to incorporate these effects in our future simulation, for instance, to impose a driven electric field at the inflow boundary on the high-density side. The results presented here would be a good start for further studying the RF in asymmetric reconnection.

This work was supported by the National Science Foundation of China (NSFC) under grant 41774154 and the Nanchang University Graduate Innovation Special Fund Project under grant CX2019058. The PIC simulations were performed by using the TH-1A supercomputer at Tianjin (nsc-tj). The simulation results used in this paper are available at https://drive.google.com/drive/folders/1r5ZWuscX8k7Xx0880VJdbJlm2QovP_PM?usp=sharing.

ORCID iDs

Liangjin Song  <https://orcid.org/0000-0003-3934-2094>

References

- Angelopoulos, V., Runov, A., Zhou, X. Z., et al. 2013, *Sci*, 341, 1478
 Birdsall, C. K., & Langdon, A. B. 1985, *Plasma Physics Via Computer Simulation* (New York: McGraw-Hill)
 Birm, J., Hesse, M., Nakamura, R., et al. 2013, *JGRA*, 118, 1960
 Burch, J. L., Torbert, R. B., Phan, T. D., et al. 2016, *Sci*, 352, aaf2939
 Cassak, P. A., & Shay, M. A. 2007, *PhPI*, 14, 102114
 Daughton, W. 1999, *PhPI*, 6, 1329
 Deng, X., Ashour-Abdalla, M., Zhou, M., et al. 2010, *JGRA*, 115, A09225
 Deng, X. H., & Matsumoto, H. 2001, *Natur*, 410, 557
 Divin, A., Khotyaintsev, Y. V., Vaivads, A., et al. 2015, *JGRA*, 120, 2675
 Drake, J. F., Swisdak, M., Cassak, P. A., et al. 2014, *GeoRL*, 41, 3710
 Fu, H. S., Cao, J. B., Khotyaintsev, Y. V., et al. 2013, *GeoRL*, 40, 6023
 Fu, H. S., Khotyaintsev, Y. V., André, M., et al. 2011, *GeoRL*, 38, L16104
 Fu, H. S., Khotyaintsev, Y. V., Vaivads, A., et al. 2012, *GeoRL*, 39, L06105
 Huang, S. Y., Fu, H. S., Yuan, Z. G., et al. 2015a, *JGRA*, 120, 4496
 Huang, S. Y., Zhou, M., Deng, X. H., et al. 2012, *AnGeo*, 30, 97
 Huang, S. Y., Zhou, M., Yuan, Z. G., et al. 2015b, *JGRA*, 120, 6188
 Hwang, K. J., Goldstein, M. L., F-Viñas, A., et al. 2014, *JGRA*, 119, 2484
 Khotyaintsev, Y. V., Cully, C. M., Vaivads, A., et al. 2011, *PhRvL*, 106, 165001
 Khotyaintsev, Y. V., Divin, A., Vaivads, A., et al. 2017, *GeoRL*, 44, 1234
 Li, H., Zhou, M., Deng, X., et al. 2015, *JGRA*, 120, 1086
 Liu, C. M., Fu, H. S., Xu, Y., et al. 2018, *GeoRL*, 45, 4628
 Liu, J., Angelopoulos, V., Runov, A., et al. 2013, *JGRA*, 118, 2000
 Malakit, K., Shay, M. A., Cassak, P. A., et al. 2010, *JGRA*, 115, A10223
 Man, H. Y., Zhou, M., Deng, X. H., et al. 2018, *GeoRL*, 45, 8729
 Nakamura, R., Baumjohann, W., Klecker, B., et al. 2002, *GeoRL*, 29, 3-1
 Ohtani, S., Shay, M. A., & Mukai, T. 2004, *JGRA*, 109, A03210
 Ono, Y., Tanabe, H., Yamada, T., et al. 2012, *PPCF*, 54, 124039
 Paschmann, G., Sonnerup, B. U. Ö., Papamastorakis, I., et al. 1979, *Natur*, 282, 243
 Priest, E. 2000, in *Magnetic Reconnection*, ed. E. Priest & T. Forbes (Cambridge: Cambridge Univ. Press), 612
 Runov, A., Angelopoulos, V., Sitnov, M. I., et al. 2009, *GeoRL*, 36, L14106
 Runov, A., Angelopoulos, V., Zhou, X. Z., et al. 2011, *JGRA*, 116, A05216
 Sitnov, M. I., Swisdak, M., & Divin, A. V. 2009, *JGRA*, 114, A04202
 Swisdak, M., Rogers, B. N., Drake, J. F., et al. 2003, *JGRA*, 108, 1218
 Vaivads, A., Khotyaintsev, Y., André, M., et al. 2004, *PhRvL*, 93, 105001
 Vapirev, A. E., Lapenta, G., Divin, A., et al. 2013, *JGRA*, 118, 1435

- Villasenor, J., & Buneman, O. 1992, [CoPhC](#), **69**, 306
- Wu, P., & Shay, M. A. 2012, [GeoRL](#), **39**, L08107
- Yee, K. S. 1966, [ITAP](#), **14**, 302
- Zenitani, S., Hesse, M., Klimas, A., et al. 2011, [PhRvL](#), **106**, 195003
- Zhou, M., Ashour-Abdalla, M., Berchem, J., et al. 2016, [GeoRL](#), **43**, 4808
- Zhou, M., Ashour-Abdalla, M., Deng, X., et al. 2009, [GeoRL](#), **36**, L20107
- Zhou, M., Deng, X. H., & Huang, S. Y. 2012a, [PhPI](#), **19**, 042902
- Zhou, M., Deng, X. H., Pang, Y., et al. 2012b, [PhPI](#), **19**, 072907
- Zhou, M., Huang, J., Man, H. Y., et al. 2019, [ApJL](#), **872**, L26
- Zhou, M., Huang, S. Y., Deng, X. H., et al. 2011, [ChPhL](#), **28**, 109402
- Zhou, M., Ni, B., Huang, S., et al. 2014a, [JGRA](#), **119**, 4335
- Zhou, M., Pang, Y., Deng, X., et al. 2014b, [JGRA](#), **119**, 6177
- Zhou, X. Z., Angelopoulos, V., Sergeev, V. A., & Runov, A. 2010, [JGRA](#), **115**, A00I03